

Lamont, T.N., Roberts, N.M.W., Searle, M.P., Gardiner, N.J., Goon, P., Hsieh, Y.-T., Holdship, P., and White, R.W., 2022, Contemporaneous crust-derived I- and S-type granite magmatism and normal faulting on Tinos, Delos, and Naxos, Greece: Constraints on Aegean orogenic collapse: GSA Bulletin, <https://doi.org/10.1130/B36489.1>.

Supplemental Material

Text. Supporting information.

Table S1. Whole Rock Geochemistry.

Table S2. Sr-Nd Isotope Results.

Table S3. Cyclades granites U-Pb zircon results.

Supporting information

Contemporaneous crust-derived 'I- and S-type' granite magmatism and normal faulting on Tinos, Delos and Naxos, Greece: constraints on Aegean orogenic collapse

Whole rock geochemistry

Major elements were analysed by X-ray Fluorescence (XRF) at the Department of Earth and Environment, Franklin and Marshall College, Pennsylvania, USA. Trace elements were measured using a PerkinElmer NexION 350D inductively coupled plasma mass spectrometer (ICP-MS) at the Department of Earth Sciences, University of Oxford. Reported precision is less than $\pm 1\%$ for major elements and $\pm 5\%$ (2.S.D.) for trace elements. The results are combined with granitoid literature data from Stouraiti et al., (2010, 2017), Altherr et al., (2002), Pe-Piper, (2000); Pe-Piper and Piper (2005).

Geochemical Sample Preparation and Methods

All samples were thoroughly washed and cleaned then crushed into a < 80 -micron powder using a Jaw crusher, followed by running through a Tema Mill using an agate crucible to avoid contamination by tungsten carbide. The crucible was thoroughly cleaned and run through separately with in house sand and the resultant powder was then passed through an 80-micron sieve. Some of the resultant powders were then sent off to the Franklin and Marshall College, Pennsylvania, USA, for X-ray fluorescence by Dr Stanley Mertzman. The remaining powder was weighed and prepared for ICP-MS in house at the Department of Earth Sciences, University of Oxford. Full descriptions for each method are outlined below.

X-Ray Fluorescence

XRF was carried out by weighing 0.4000 ± 0.0001 grams of crushed rock powder and mixing with lithium tetraborate (3.6000 ± 0.0002 grams). The subsequent solution was then placed in a platinum crucible and heated with a meeker burner until molten. The molten material was transferred to a platinum casting dish and quenched. This procedure produced a glass disk that is used for XRF analysis of SiO_2 , Al_2O_3 , CaO , K_2O , P_2O_5 , TiO_2 , total iron reported as $\text{Fe}_2\text{O}_3\text{T}$, MnO , Na_2O and MgO . Trace element analysis was achieved by weighing 7.0000 ± 0.0004 grams of whole rock powder and adding 1.4000 ± 0.0002 of high purity copolywax powder. This was mixed for 10 minutes, and the powder was pressed into a briquette. Data are reported as parts per million (ppm) for Rb, Sr, Y, Zr, Nb, Ni, Ga, Cu, Zn, U, Th, Co, Pb, Sc, Cr, V, La, Ce, and Ba. Working curves for each element were determined by analyzing geochemical rock standards Abbey (1983) and Govindaraju (1994). Between 30 and 50 data points were gathered for each working curve; various element interferences are also taken into account. Results were calculated and presented as percent oxide. The amount of ferrous Fe was determined by the titration using a modified Reichen and Fahey (1962) method which includes weighing out 0.5000 ± 0.0002 grams of sample powder and transfer to a large alumina crucible and cover, 5 ml of deionized H_2O , 5 ml of concentrated H_2SO_4 , were added followed by 5 ml of HF directly into each alumina crucible which were immediately covered and heated over Meker burner until felt to be boiling. Once sufficiently boiling, the crucible was removed and allowed to stand for 10 minutes. 450 ml of the boric acid solution was then added to an 800 ml plastic beaker, one beaker for each crucible, then 3-5 drops of 3.0% Sodium diphenylamine sulfonate solution was added as an indicator. After the crucible was heated for 10 minutes, it was picked up and placed to the bottom of the beaker,

so it is covered by solution. This solution was then promptly titrated using a standard solution of $K_2Cr_2O_7$ (potassium dichromate) to a purple end point, the amount of $K_2Cr_2O_7$ used in ml*0.8 is the weight % FeO of the sample, weight %Fe₂O₃ was determined by division by 1.111348 to give %FeOT, then %FeOT-%FeO (titrated)=Fe₂O₃, then Fe₂O₃*1.111348 = weight %Fe₂O₃. Loss on ignition is determined by heating an exact aliquot of the sample at 950 °C for one hour.

Trace element geochemistry (ICP-MS)

All sample powders were weighed to approximately 100 ± 0.1 mg and then diluted and digested over 7 days in vials using 2 ml of concentrated HF and 4ml of HNO₃ at 80 °C and evaporated at 90 °C. Two 2 ml's of HNO₃ was then added and evaporated to dry then 1-3 ml of 16 M HNO₃ was added with MilliQ. The samples were then heated overnight and diluted to 10 ml making a concentration of 2 M HNO₃ in the final solution. 2 M HNO₃ was then added to make up 48 ml of solution. Stock calibrations for standards A were made by adding 0.5 ml of 10 ppm solutions of transition, alkali, REE's and HFS standards making a result solution of 50 g. Stock calibration for standards B were made by using 48.5 ml of 2 M HNO₃ with 0.5 ml of stock calibration standard A then 0.5 ml of each QCA and QCB were added to make up to 50 ml. Three internal standards were used including In, Rh and Re, and six runs of all element standards was collected. The subsequent standard results are presented in Table S4 and reported data as ppm concentrations. A spectrum of trace elements was collected on a Perkin Elmer 6100DRC Quadrupole inductively coupled plasma mass spectrometer (ICP-MS) with a dynamic reaction cell at the Department of Earth Sciences, University of Oxford. Measured elements from whole rock samples include Sc, Y, Cs, La, Ce, Pr, Nd, Sm, Eu, Gd, Tb, Dy, Ho, Er, Tm, Yb, Lu, Th, U, Co, Ga, Nb, Mo, Hf, W, Pb

Standards data														
	Sc 45	Y 89	In 115 (IS)	Cs 133	La 139	Ce 140	Pr 141	Nd 143	Sm 147	Eu 153	Gd 157	Tb 159	Dy 163	Ho 165
	ng/g	ng/g	IS	ng/g	ng/g	ng/g	ng/g	ng/g	ng/g	ng/g	ng/g	ng/g	ng/g	ng/g
S7_R1	2.23189	2.12256	0.95859	1.99721	2.10434	2.13118	2.05070	2.03105	2.07463	2.12847	2.03198	2.07067	2.05250	2.09948
S7_R2	2.29585	2.15303	0.97428	1.98981	2.14026	2.15226	2.05217	2.01212	2.10287	2.16759	2.05832	2.11047	2.08219	2.13980
S7_R3	2.17058	2.06831	0.97481	2.00193	2.09096	2.11257	2.02768	2.03948	2.03855	2.10821	1.99033	2.05810	2.01083	2.07621
S7_R4	2.15955	2.16036	0.98668	2.01298	2.12063	2.12246	2.05548	2.07542	2.07381	2.13512	2.01031	2.07614	2.04403	2.13129
S7_R5	2.20374	2.16287	0.98535	1.99965	2.11632	2.12012	2.05952	2.08417	2.10603	2.13282	2.03274	2.07306	2.03881	2.11836
S7_R6	2.16727	2.10186	0.97290	1.98527	2.08619	2.09555	2.01406	2.01496	2.02217	2.08632	2.01250	2.03081	2.00375	2.08123
Precision														
	ng/g	ng/g	IS	ng/g	ng/g	ng/g	ng/g	ng/g	ng/g	ng/g	ng/g	ng/g	ng/g	ng/g
AVG	2.20	2.13		2.00	2.11	2.12	2.04	2.04	2.07	2.13	2.02	2.07	2.04	2.11
STD	0.05	0.04		0.01	0.02	0.02	0.02	0.03	0.03	0.03	0.02	0.03	0.03	0.03
RSD%	2.37	1.78		0.49	0.96	0.89	0.89	1.49	1.63	1.29	1.16	1.25	1.41	1.25
2*RSD%	4.74	3.56		0.97	1.91	1.78	1.77	2.98	3.26	2.58	2.32	2.51	2.81	2.50
Accuracy														
	ng/g	ng/g	IS	ng/g	ng/g	ng/g	ng/g	ng/g	ng/g	ng/g	ng/g	ng/g	ng/g	ng/g
Check std conc	2.09429	2.04943		1.99892	2.08386	2.12121	2.05193	2.04003	2.08260	2.11015	2.04880	2.08761	2.06236	2.12789
Percentage of theoretical	105.28	103.84		99.94	101.24	100.05	99.58	100.14	99.38	100.77	98.73	99.15	98.85	99.05
Accuracy %	5.28	3.84		0.06	1.24	0.05	0.42	0.14	0.62	0.77	1.27	0.85	1.15	0.95

Table S4: ICP-MS Trace element geochemistry standards data

Table S4 continued:

Er 166	Tm 169	Yb 173	Lu 175	Th 232	U 238	Co 59	Ga 69	Nb 93	Mo 98	Rh 103 (IS)	Hf 178	W 182	Re 185 (IS)	Pb 208
ng/g	ng/g	ng/g	ng/g	ng/g	ng/g	ng/g	ng/g	ng/g	ng/g	IS	ng/g	ng/g	IS	ng/g
2.05135	2.07743	2.07928	2.08074	1.99093	1.96080	2.06698	2.01803	2.04911	2.02212	0.96318	1.96496	2.03276	0.98058	2.00775
2.07474	2.09847	2.11434	2.10355	2.01888	1.98845	2.11039	2.05012	2.10089	2.11239	0.97257	2.06856	2.06857	0.98015	2.02596
2.03931	2.05753	2.03019	2.04705	1.93240	1.91341	2.01031	2.01237	2.03181	2.01988	0.98083	1.98163	1.65249	0.98173	1.97203
2.06576	2.08546	2.08106	2.07429	1.95992	1.93681	2.06401	2.03817	2.06354	2.05236	0.98697	2.04543	1.61265	0.99959	1.99152
2.08116	2.07307	2.11042	2.06808	1.94343	1.92620	2.08132	2.02864	2.09403	2.08655	0.97804	2.02235	1.82121	0.98253	2.02221
2.01258	2.03213	2.05449	2.03437	1.91739	1.89943	2.05658	2.04002	2.02427	2.02277	0.96808	2.00170	1.74613	0.98525	1.93630
ng/g	ng/g	ng/g	ng/g	ng/g	ng/g	ng/g	ng/g	ng/g	ng/g	IS	ng/g	ng/g	IS	ng/g
2.05	2.07	2.08	2.07	1.96	1.94	2.06	2.03	2.06	2.05		2.01	1.82		1.99
0.03	0.02	0.03	0.02	0.04	0.03	0.03	0.01	0.03	0.04		0.04	0.19		0.03
1.24	1.12	1.55	1.19	1.95	1.68	1.59	0.70	1.54	1.90		1.94	10.51		1.71
2.48	2.25	3.11	2.38	3.89	3.36	3.18	1.41	3.08	3.80		3.88	21.03		3.42
ng/g	ng/g	ng/g	ng/g	ng/g	ng/g	ng/g	ng/g	ng/g	ng/g	IS	ng/g	ng/g	IS	ng/g
2.07509	2.08866	2.09575	2.10639	2.02981	2.03203	2.02458	2.00829	2.04909	2.03973		2.03302	2.03973		2.01332
98.99	99.14	99.17	98.18	96.58	95.35	101.99	101.14	100.56	100.63		99.07	89.34		98.97
1.01	0.86	0.83	1.82	3.42	4.65	1.99	1.14	0.56	0.63		0.93	10.66		1.03

Sr-Nd isotopes

Column chemistry

Digested samples were converted into 2M HNO₃, and 1mL of the dissolved solution was taken to perform Sr and Nd purification using a single-stage separation of Sr and Nd by the ESI PrepFast-MC Sr-Ca column before the Sr and Nd isotope measurements. The method was modified from Romaniello et al. (2015) and Retzmann et al. (2017). To achieve high recovery, Ca contain is kept below 200 µg in the sample solution for the column chemistry. The column chemistry elution curves were calibrated with the USGS standard BCR-1, containing ~1300 ng Sr and ~110 ng Nd. The calibration result is shown in Fig. S1. The purified Sr and Nd solutions were dried at 100°C and re-dissolved in 2mL 2% HNO₃ prior to the isotopic analysis. The total procedure blank was < 0.3 ng Sr and < 0.05 ng Nd, which contributes < 0.1% of the total Sr and Nd in each sample.

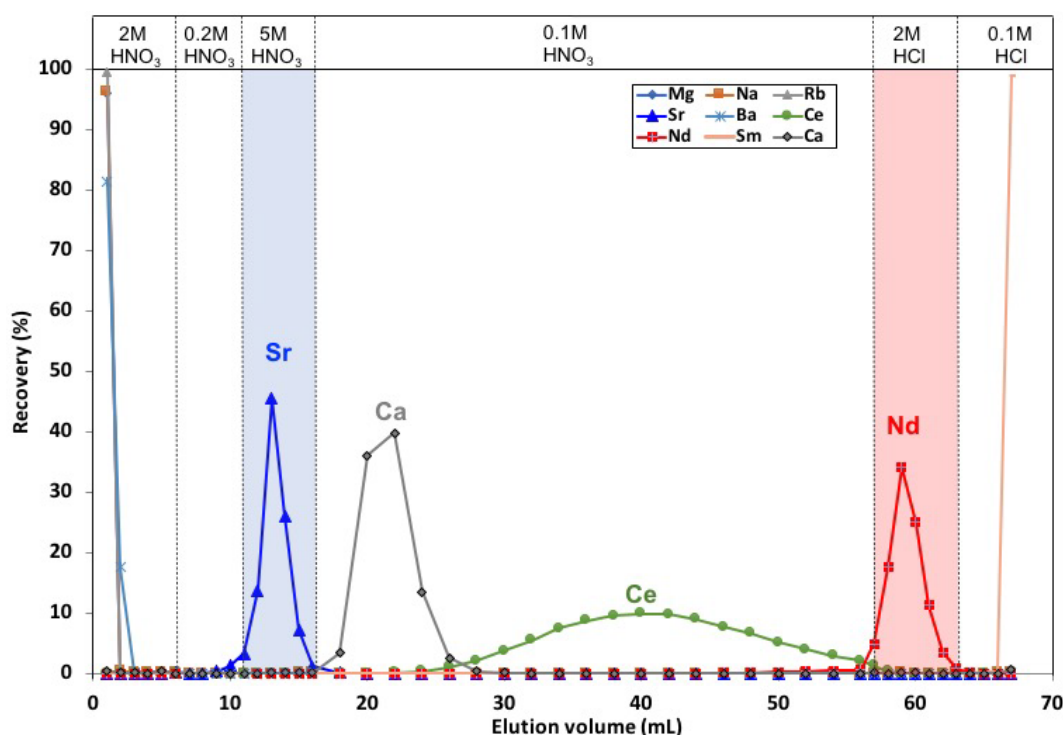


Figure S1. Elution curves of Sr and Nd purification procedures using different reagents in the PrepFast-MC Sr-Ca column. The column bed volume is 1mL.

MC-ICP-MS mass spectrometry

The Sr and Nd isotope measurements were performed on a Nu Plasma multi-collector inductively coupled plasma mass spectrometer (MC-ICP-MS) in the Department of Earth Sciences, University of Oxford. The instrument was coupled with a membrane desolvating system (AridusII, Cetac) to achieve high signal sensitivity and stability.

Sr isotopes

Samples were measured using a standard bracketing method with the NIST SRM 987 standard. Each sample was repeated three times. The instrument mass fractionation was corrected internally using $86\text{Sr}/88\text{Sr} = 0.1194$. In Table S5, all reported $87\text{Sr}/86\text{Sr}$ ratios have been normalised to SRM987 $87\text{Sr}/86\text{Sr} = 0.710248$ (McArthur et al., 2001). The external reproducibility of $87\text{Sr}/86\text{Sr}$ in SRM 987 yielded a value of 0.710251 ± 0.000025 (2SD, $n=30$). In Table S5, three USGS standards (G-2, BCR-1 and BHVO-2) were also measured for comparison, and the values are consistent with the reference values reported in previous studies (e.g. Weis et al., 2006).

Nd isotopes

Samples were measured by bracketing with the JNdi-1 Nd isotope standard. Each sample was repeated three times. The instrument mass fractionation was corrected internally using $146\text{Nd}/144\text{Nd} = 0.7219$. The instrument drift was corrected by normalizing $143\text{Nd}/144\text{Nd}$ ratios to the bracketing standard JNdi-1 with a reference ratio of 0.512115 (Tanaka et al., 2000). Repeated measurements of $143\text{Nd}/144\text{Nd}$ in JNdi-1 yielded a value of 0.512117 ± 0.000017 (2SD, $n=18$). In Table S5, the measured values of three USGS standards (G-2, BCR-1 and BHVO-2) were also reported for comparison.

Table S5: USGS standard Sr and Nd isotope data

USGS ID	$^{87}\text{Sr}/^{86}\text{Sr}$	2SD (n=3)	$^{87}\text{Sr}/^{86}\text{Sr}^*$	2SD
G-2	0.709761	0.000032	0.709770	0.000014
BCR-1	0.705018	0.000004	0.705018	0.000013
BHVO-2	0.703471	0.000023	0.703479	0.000020
	$^{143}\text{Nd}/^{144}\text{Nd}$	2SD (n=3)	$^{143}\text{Nd}/^{144}\text{Nd}^*$	2SD
G-2	0.512212	0.000042	0.512235	0.000015
BCR-1	0.512642	0.000021	0.512646	0.000016
BHVO-2	0.512949	0.000038	0.512990	0.000010

*Reference values from Weis et al. (2006)

U-Pb geochronology

U-Pb sample preparation and geochronology methods

All analytical work was carried out at the Geochronology and Tracers Facility, British Geological Survey, Keyworth, Nottingham. All samples were crushed using standard techniques (Jaw-crushing, disc milling, sieving, Rogers table, heavy liquids, Frantz magnetic separation). Approximately 5-10 kg of each sample was crushed to ensure sufficient extraction of enough zircon. Zircons from each successful sample were then picked under alcohol and mounted in 1-inch epoxy resin mounts and polished until all grains were exposed. All imaging was performed on a FEI Quanta 600 ESEM. Complexities in zircon growth patterns were identified prior to analysis by careful cathodoluminescence CL imaging of zircon grains. Locations of ablation spots for geochronological work were chosen to ensure separate domains could be analysed, therefore minimizing the potential mixing of different ages. Some zircon grains were analysed by placing the grains on double-sided tape, after rinsing with weak nitric acid, and ablating directly on the surface of the grains. The dated zircons are primarily new igneous zircons for the I-type granitoids (although there were some inherited grains with older xenocrystic cores), in contrast most of the S-type granites have inherited cores with Variscan or older ages (Fig. 10b).

Zircon grains were successfully extracted from key granitoid samples. For sample locations see Figs. 2, 4 and 5 and Table S7 below. Cathodoluminescence images of zircon grains are presented in Fig. S2.

U–Pb geochronology was conducted using a Nu Instruments Attom HR sector-field single-collector inductively coupled plasma mass spectrometer (SC-ICP-MS). Laser ablation was performed with a New Wave Research 193UC laser ablation system, using a New Wave Research TV2 cell; this features a moveable cup with an ablation volume of ca. 1 cm³. The analytical protocol is previously described for zircon (Spencer et al., 2015). A standard-sample-bracketing technique was used to normalise the data, this involved calculation of normalisation factors based on the measured/accepted value for the ²⁰⁷Pb/²⁰⁶Pb and ²⁰⁶Pb/²³⁸U ratios of the reference material, analysed at regular intervals during each session. The Nu Attom ICP-MS was used in peak-jumping mode with measurement on a MassCom secondary electron multiplier (SEM). The following masses were measured in each sweep: ²⁰²Hg, ²⁰⁴Pb+Hg, ²⁰⁶Pb, ²⁰⁷Pb, ²⁰⁸Pb, ²³²Th, and ²³⁵U. Each data integration records 80 sweeps of the measured masses, which roughly equates to 0.3 seconds. Because ²³⁵U is measured, ²³⁸U is calculated from ²³⁵U *137.818 (Hiess et al., 2012).

Laser ablation parameters were 15 µm or 25 µm (depending on the session) static spots, a fluence of 2.0–2.5 J/ cm², an ablation time of 20 s, a repetition rate of 5 Hz, and a 5 s washout between ablations. A 60 s on-peak gas blank is taken before every set of standard and sample ablations. U–Pb data were normalized to the average ‘normalization factor’, i.e. drift-corrected measured/accepted value, for a combination of zircon reference materials comprising 91500, GJ-1 and Plešovice.

A ²⁰⁷Pb based common lead correction utilises the measured ²⁰⁷Pb/²⁰⁶Pb ratios, and an assumed ²⁰⁷Pb/²⁰⁶Pb ratio of common lead to calculate the proportion of common ²⁰⁶Pb. This correction assumes that the U–Pb data are concordant and is useful in young grains where accurate knowledge of the ²⁰⁶Pb/²³⁸U is required. The Stacey and Kramers (1975) model composition is used in calculating these common lead corrections and an initial age estimate is based on regression in a Tera–Wasserburg diagram. Another correction is made to the common-lead corrected ages to account for any excess ²⁰⁶Pb that is derived from ²³⁰Th, an intermediate daughter nuclide of the ²³⁸U decay series. This correction involves estimation of the whole-rock Th/U ratio at 3.8. For full analytical conditions please consult the Table S3 below.

Data processing used the time-resolved analysis on the Nu Instruments’ software, an in-house Excel spreadsheet for data reduction and uncertainty propagation (after Horstwood et al., 2016), Isoplot (Ludwig, 2003), and IsoplotR, (Vermeesch, 2018) for data presentation. All data are plotted at the 2σ confidence interval.

Table S6: Full laboratory and analytical procedures	
Laboratory and Sample Preparation Table	
Laboratory Name	Geochronology and Tracers Facility
Minerals analysed	Zircon
Sample preparation	Whole rock, heavy liquid and magnetic separation (Zircon)
Imaging	Cameca 600 FEI Quanta SEM with WDS capability (BGS, Keyworth)
Laser ablation system	
Make model and type	ESI/ New Wave Research 193UC
Ablation and cell volume	NWR TV2; washout time < 1sec.
Laser wavelength (nm)	193 nm

Pulse width (ns)	3-4 ns
Fluence (J cm⁻²)	~2.5 J cm ⁻²
Repetition rate (Hz)	5 Hz
Ablation duration (Sec)	Variable, see text
Ablation pit depth/ ablation rate	~12 µm on standard zircon ablation (30 s)
Spot size	
Zircon	10-25 µm
Sampling mode/ pattern	Static spot ablation
Carrier gas	100% He, Ar make-up gas combined ca.50% along sample line.
Cell carrier gas flow (l/min)	0.8l/min 0.7l/min
ICPMS Instrument	
Make model and type	Nu Instruments Attom SC-SF-ICP-MS
Sample introduction	Free air aspiration of desolvator
RF power (W)	1300W
Make-up gas flow (l/min)	0.8l/min Ar
Detection system	Discrete dynode MassCom ion counter
Masses measured	202, 204, 206, 207, 208, 232, 235
Integration time per peak	200µs (202, 204, 206), 400µs (232, 208), 1000µs (207, 235) 80 sweeps per integration
Total integration time per reading (secs)	0.30 seconds
Sensitivity / Efficiency (% , element)	~0.2% for Uranium
IC Dead time (ns)	15ns
Data Processing	In-house spreadsheet, Nu TRA software
Gas blank	60 second on-peak zero subtracted
Calibration strategy	
Zircon	91500 (Wiedenbeck et al., 1995) used as primary reference material, GJ-1 (Jackson et al., 2004) and Plešovice (Sláma et al., 2008) used as secondary references materials.
Data processing package used / Correction for LIEF	Nu Instruments TRA acquisition software, in-house spreadsheet data processing
Mass discrimination	²⁰⁷ Pb/ ²⁰⁶ Pb and ²⁰⁶ Pb/ ²³⁸ U normalised to reference material
Common-Pb correction, composition and uncertainty	Stacey & Kramers (1975) model composition, based on f206c, using estimated age derived from ²⁰⁶ Pb/ ²³⁸ U
Uncertainty level & propagation	Ages in the data table are quoted at 2sigma absolute, propagation is by quadratic addition. Excess variance of reference material is propagated.

Quality control / Validation	See below for validation results of standards. Reproducibility and accuracy on standards for all sessions ~3% or under.
-------------------------------------	---

Reproducibility of Standards

U–Pb results of standards are summarized in Table S7 below and in Table S2 with all the U-Pb data:

Table S7: Reproducibility of U-Pb standards

<i>Mineral</i>	<i>Ref Mat.</i>	<i>²⁰⁶Pb/²³⁸U Age</i>	<i>2s</i>	<i>MSWD</i>	<i>n</i>
Session 1	Tinos, Delos, Naxos (17TL106)	granites			
Zircon	91500	1054.5	6.2	1.8	39/39
Zircon	Ples	337.8	1.4	1.1	39/39
Zircon	GJ-1	604.5	2.8	1.4	39/39
Session 2	Naxos Leucogranites				
Zircon	91500	1053.7	3.5	1.1	68/68
Zircon	Ples	339.2	1.0	0.9	67/67
Zircon	Qinghu	160.0	0.8	1.1	37/41

U-Pb Results

The results are presented in Table S2 and Fig. 11, but summary Tera-Wasserburg and weighted mean plots for each sample are presented below in figures S3 to S7.

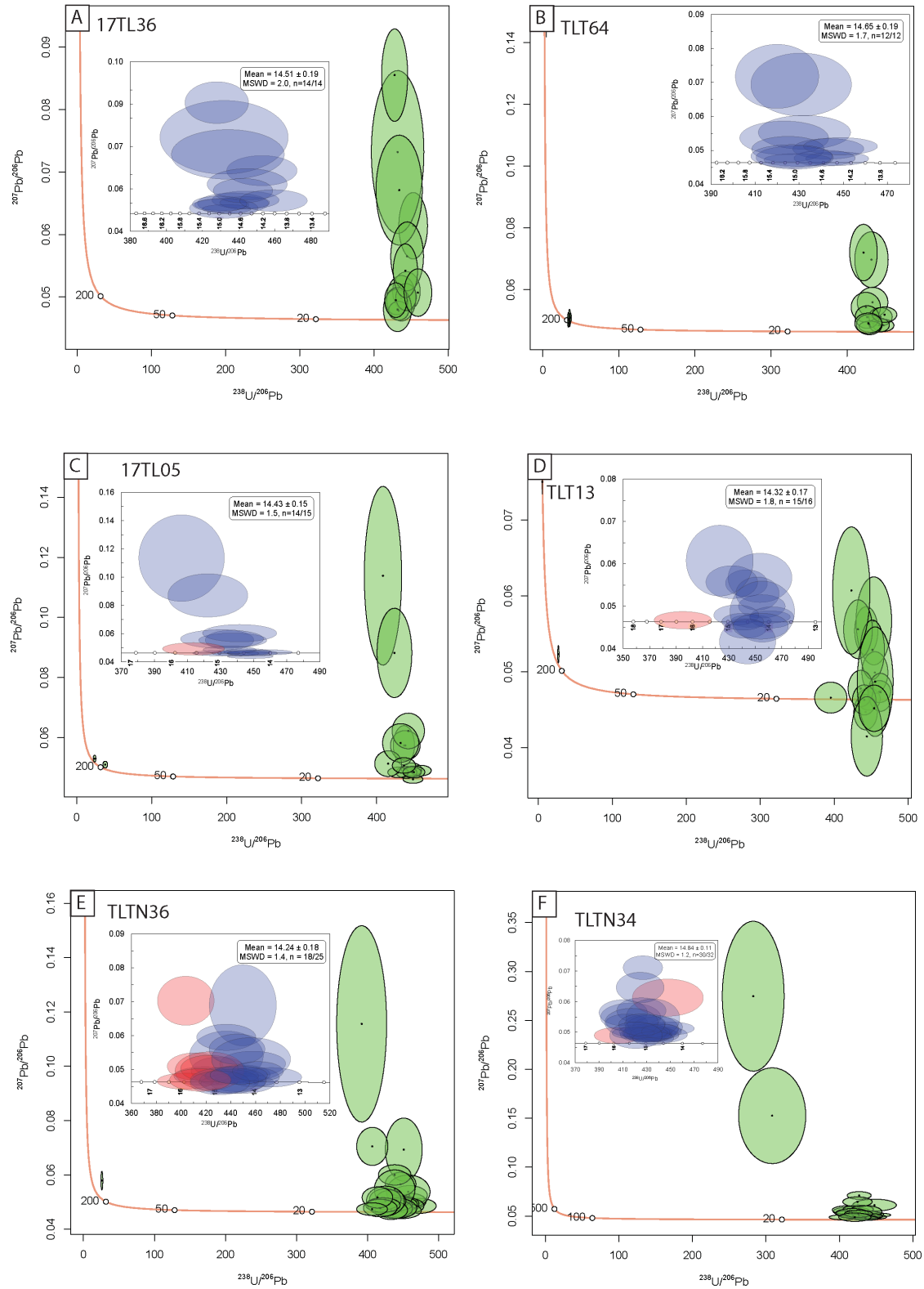


Figure S3: Tera-Wasserburg plots for I-type granitoid samples from Tinos. A, B, C) Dacite dykes, D) Aplite vein, E and F) Monzogranite pluton. Insets show the zoomed in distribution of Miocene dates and rejected analyses from lower intercept age calculation (red ellipses).

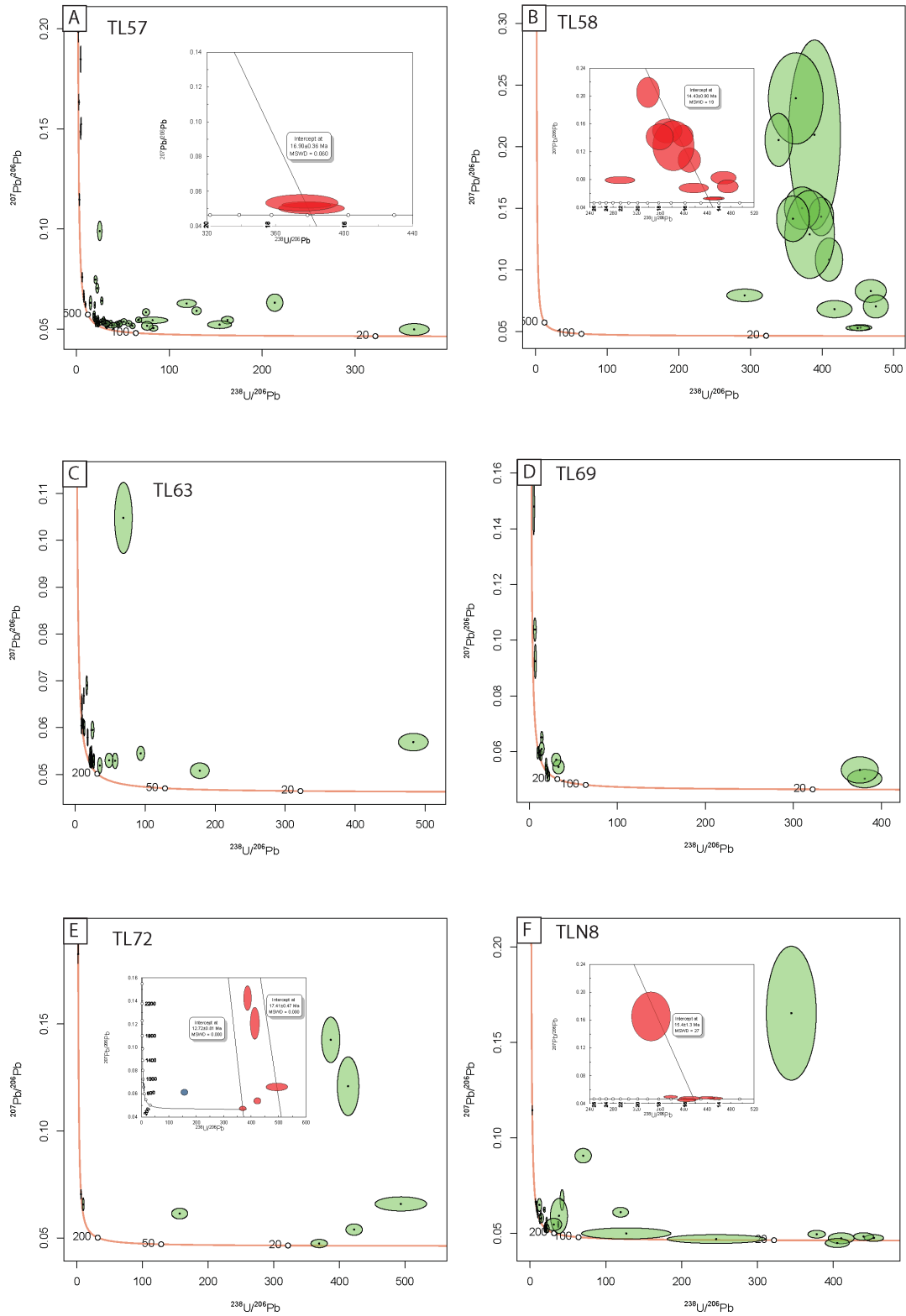


Figure S4: Tera-Wasserburg plots for Naxos S-type granite samples with insets showing distribution of Miocene ages. A) Orthogneiss basement, B-F) S-type leucogranite dykes and sills. See text for structural interpretation of age and timing of deformation.

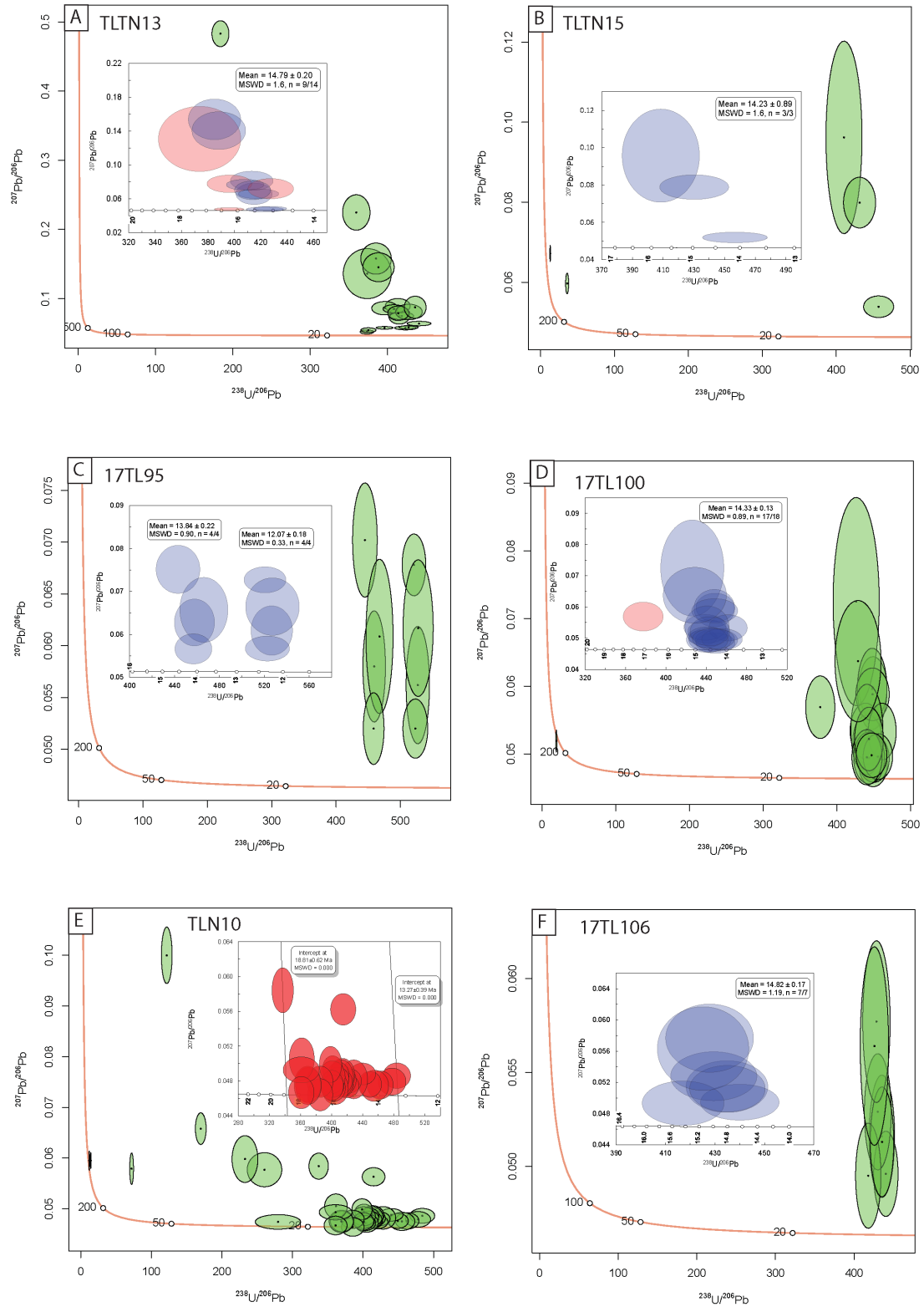


Figure S5: Tera-Wasserburg plots with inset zoomed in plots for Miocene ages for A and B) Tinos Grt-Ms S-type granites, C) Delos S-type granite, D) Tinos cross-cutting leucogranite at Livada Bay E) Naxos S-type granite, F) Aplite within the Naxos granodiorite.

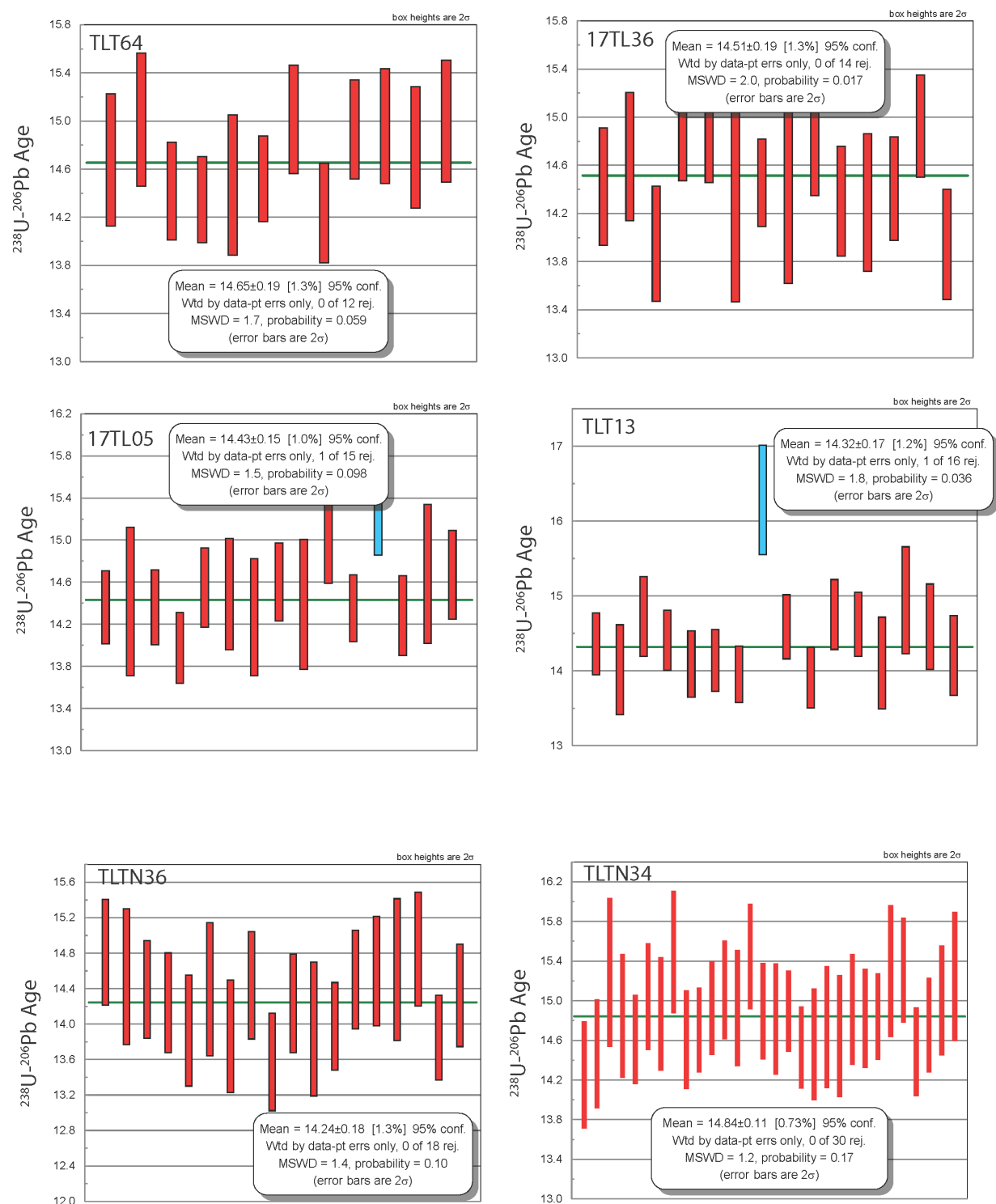


Figure S6: Weighted mean box plots for Tinos I-type granitoid samples, with blue boxes represented rejected analyses from age calculation.

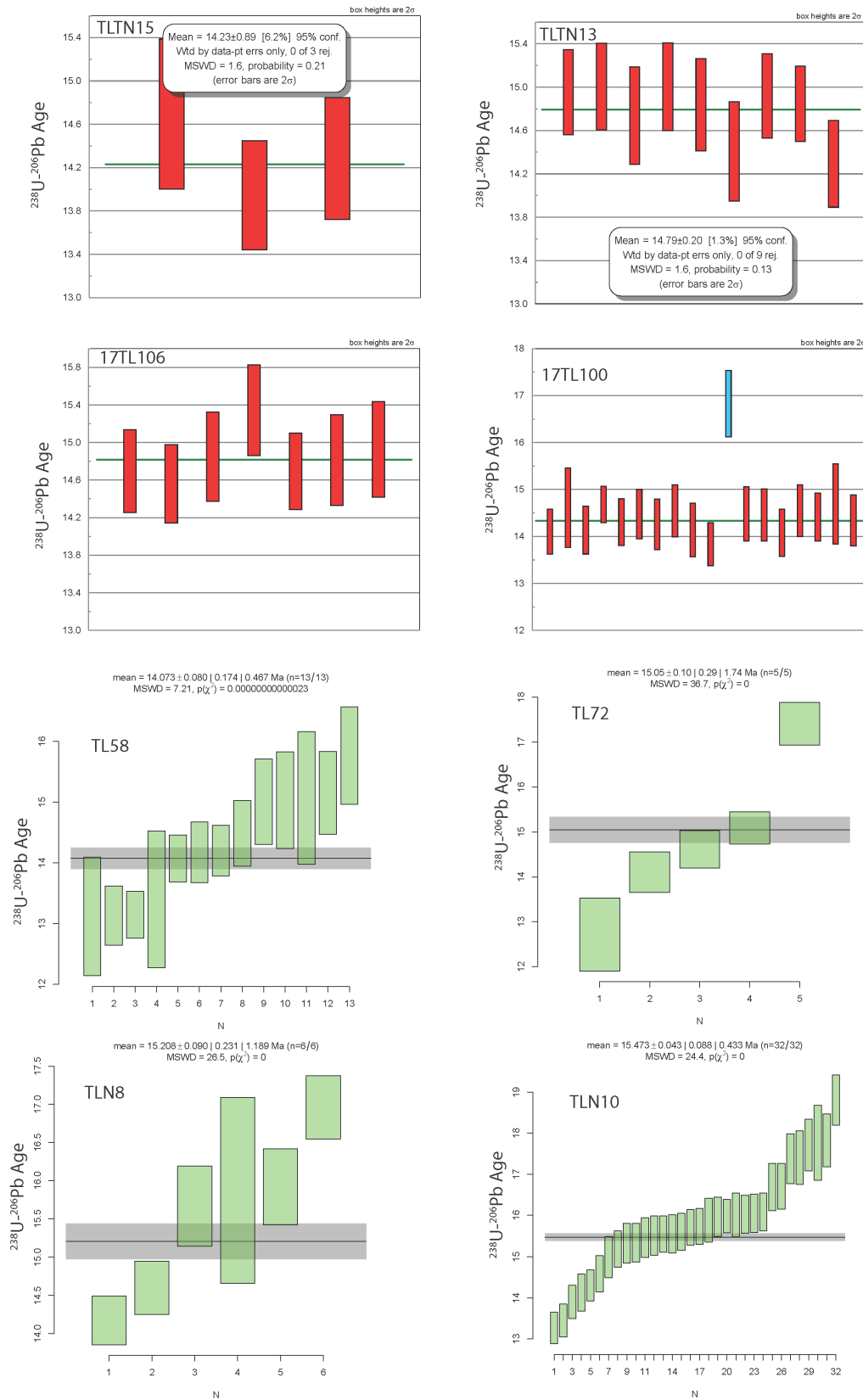


Figure S7: Weighted mean box plots for Tinos and Naxos S-type granites with blue boxes representing rejected analyses.

Additional Sm-Nd Model Age calculations

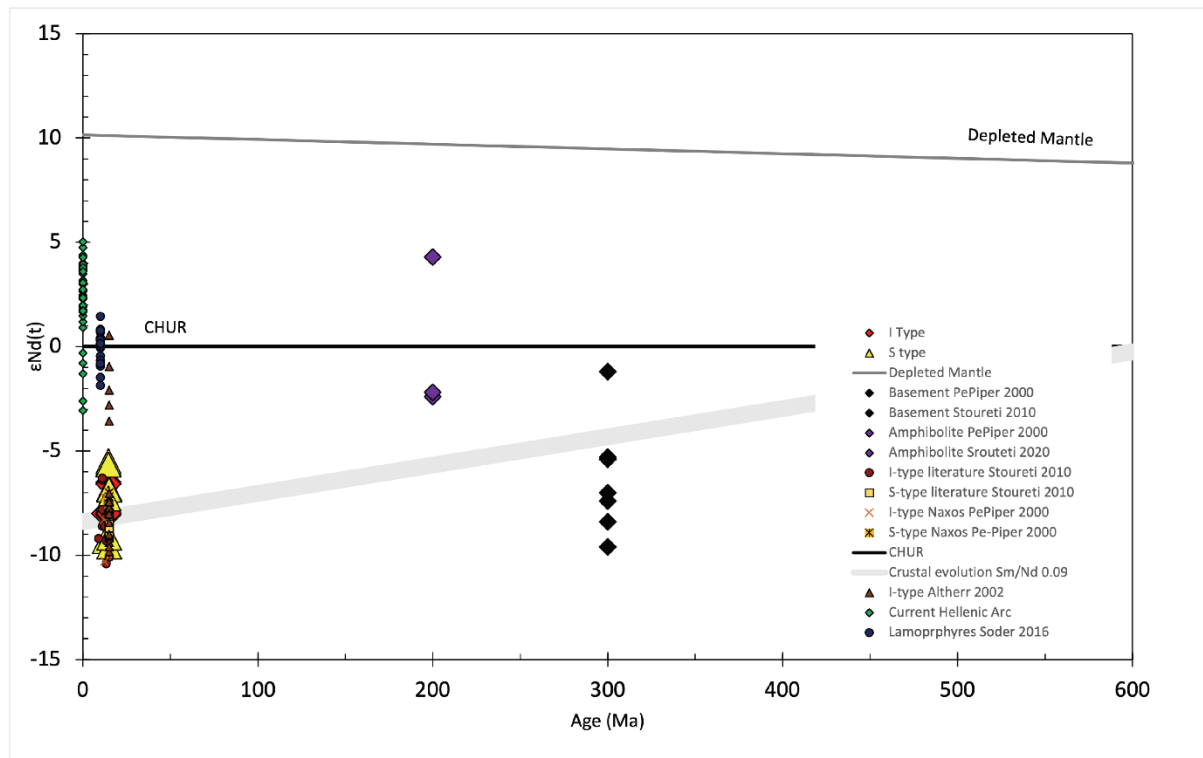


Figure S8: Sm-Nd – time evolution plot showing Miocene I- and S-type granites plot approximately on the same Nd evolution trajectory as the Variscan Basement and significantly different to the current Hellenic arc and Kos lamprophyres.

Additional Geochemical Plots

Harker Diagrams

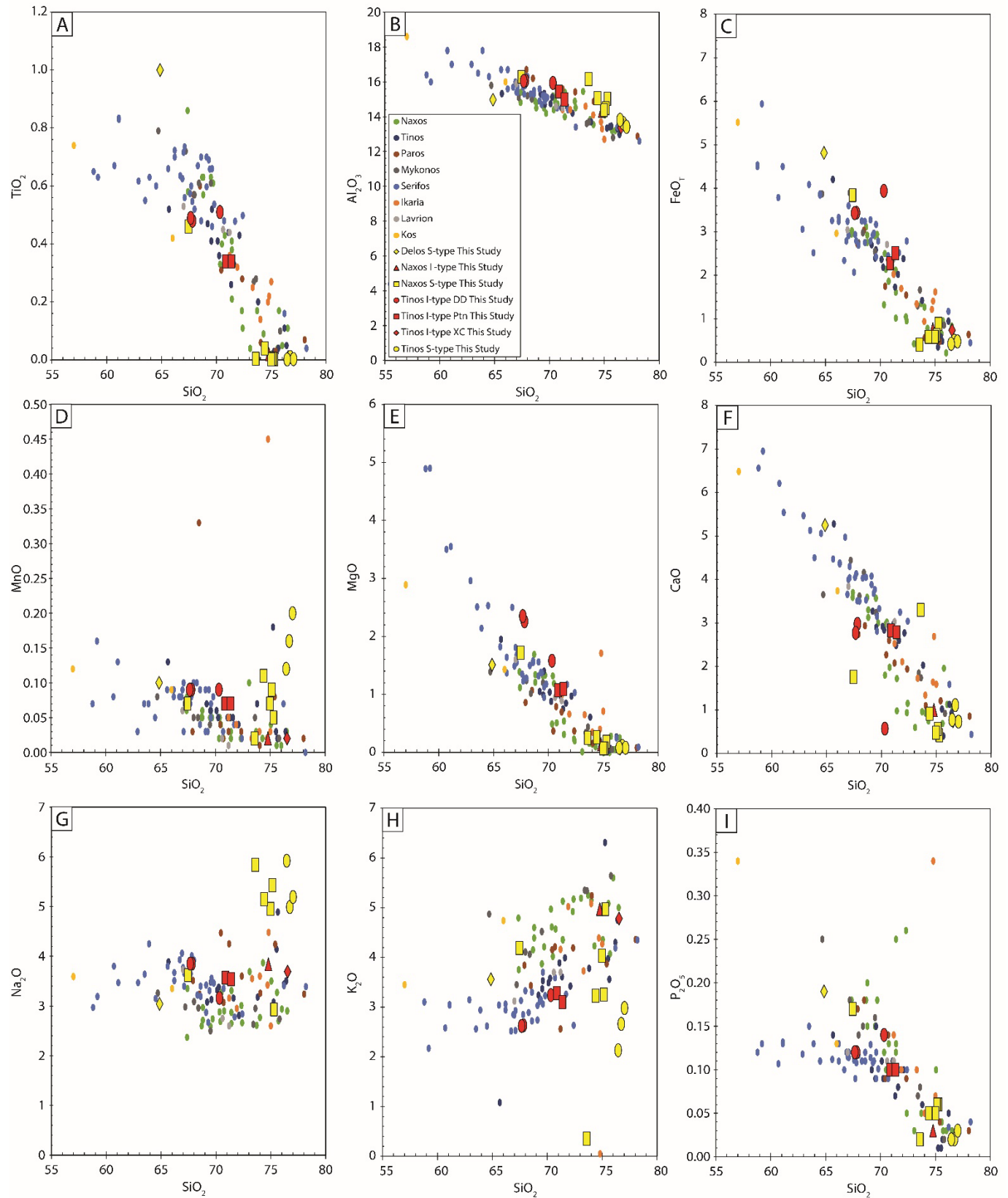


Figure S9: Harker Diagrams for the Cycladic I- and S-type granites

Granite Discrimination Diagrams

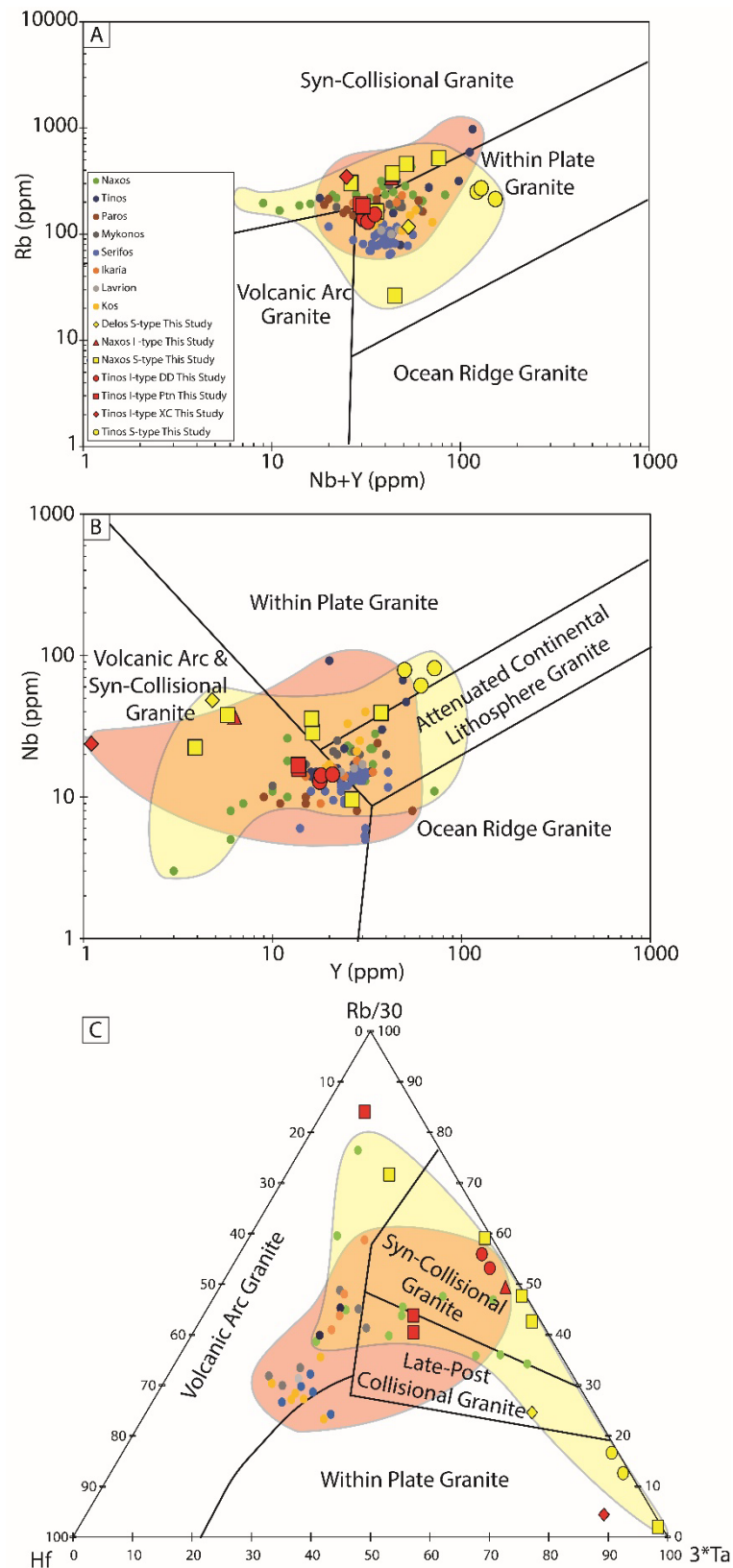


Figure S10: A) Nb vs Y granite discrimination diagram of (Pearce et al., 1984), B) Rb vs Y+Nb granite discrimination diagram (Pearce et al., 1984), C) Rb/30–Hf–3Ta ternary plot to discriminate granite types (Harris et al., 1986).

Sample Descriptions

Tinos Samples

Tinos Monzogranite Samples

TLTN36 is from the undeformed centre of the monzogranite (N37.596171, E25.197489), with no preferred alignment of hornblende and biotite, K-feldspar and plagioclase phenocrysts. Because the pluton cross-cuts the TSZ and is mostly undeformed, the age of TLTN36 constrains the end of pervasive top-to-NE shearing on the TSZ.

TLTN34 was taken from the southwestern margin of the monzogranite pluton (N37.582732, E25.175706) and is highly foliated, with a shallowly NE-plunging lineation of plagioclase and quartz that form stretching fabrics towards the NE, placing a lower age limit on ductile deformation on the TSZ.

TLT13 is a few centimetre-wide hornblende-biotite granite vein that intrudes into meta-cherts from the Mirsini Unit in the Upper Unit (N37.583181, E25.20910), possibly related to the monzogranite a few hundred meters away.

Tinos Dacite Dyke Samples

TLT64 is taken from a partially deformed dacite dyke that intrudes amphibolites of the metamorphic sole in the Upper Unit to the NE of Kolimpithra Bay (N37.628196, E25.164215) and dips towards the southeast. The date of crystallization provides a lower age bracket for movement on the TSZ, as the dyke intrudes across it. However, the dyke shows solid-state ductile deformation, indicated by partial recrystallization of plagioclase and quartz.

17TL36 is coarse-grained undeformed dacite dyke intrudes through the Moho Transition Zone sequence of alternating serpentinites and gabbros of the Tsiknias Ophiolite on the eastern flank of Mt Tsiknias (N37.580526, E25.23496). The crystallization age provides a minimum age for ductile deformation along the TSZ.

17TL05 is from a more evolved dyke that intrudes eclogite and blueschist facies rocks of the Kionnia Thrust (in the Lower Unit; Lamont et al., 2020b) at Kionnia Bay (N37.553558, E25.134661). The dyke dips moderately towards the NE and cross-cuts blueschist-facies thrust related top-to-SW fabrics, and retrograde greenschist facies top-to-NE fabrics (Lamont, 2018).

Tinos Leucogranite Samples

TLTN13 is from a garnet-muscovite leucogranite sill (N37.612741, E25.242176) that intrudes parallel to the amphibolite country rock obduction related foliation, and is cross-cut by brittle high angle normal faults. The crystallization age constrains an upper limit on the timing of brittle normal faulting that post-dates the major phase of ductile deformation on Tinos.

TLTN15 is from an adjacent leucogranite sill (N37.613210, E25.244438) that displays minor curvature into alignment with some of the normal faults (Fig. 3k,l), suggesting it crystallised shortly prior to normal faulting.

Naxos Leucogranite Samples

TL57 is a hornblende-biotite k-feldspar orthogneiss from the SW margin of the migmatite dome within the Koronos Shear Zone and is believed to represent the basement to the island. It is affected by strong recrystallization and grain boundary migration of quartz and feldspar with a pronounced NNE-SSW stretching lineation of hornblende and biotite.

TL58 is a garnet biotite leucogranite dyke that intrudes through the KSZ on the eastern margin of the migmatite dome and clearly cross-cuts the kyanite-sillimanite top-to-NNE shear fabrics. The leucogranite can clearly be traced from the structurally deeper migmatites, and into the overlying Koronos Unit. Because the granite is undeformed, the age of granite crystallization therefore constrains final movement on the KSZ.

TL63 is a garnet tourmaline leucogranite dyke that intrudes parallel to the steep westerly dipping foliation on the western margin of the migmatite dome associated with the NPDS, near the village of Kourachari. The dyke locally cross cuts the KSZ metamorphic foliation in the country rock, but is affected by post-crystallization deformation along strike, suggesting it post-dates KSZ shearing at deeper structural levels, but is synchronous with top-to-NNE shearing on the NPDS.

TL69 is a biotite-muscovite leucogranite from the western margin of the migmatite dome that is aligned parallel to the metamorphic foliation associated with the KSZ. The age of granite crystallization thus constrains the timing of top-to-NNE shearing on the KSZ.

TL72 is a deformed garnet tourmaline leucogranite sill that intrudes metasediments and a thin slither of serpentized peridotite on the NW flank of the migmatite dome. The granite intrudes from the

migmatites through the KSZ into the overlying NPDS ductile shear zone on the western margin of the migmatite dome and has been boudinaged by strong top-to-NNE shearing associated NPDS. The age granite crystallization therefore places a maximum age of NPDS shearing and a minimum age for movement on the KSZ.

TLN8 is a vertically orientated and boudinaged biotite muscovite leucogranite dyke that intrudes marble in the CHSZ. The boudinage appears to be syn granite crystallization, due to lobate margins on the granite. The age of crystallization will therefore constrain the timing of horizontal constrictional stress, associated with a vertical extension direction.

TLN10 is a horizontally NNE-SSW boudinaged garnet biotite leucogranite that also intrudes marble in the CHSZ. The NNE-SSW boudinage appears to have occurred under solid state conditions, and therefore the crystallization age will serve as an upper bound for the timing of NNE-SSW extension.

17TL106 is from an uprightly folded aplite within the interior of the Naxos I-type granodiorite (N37.074694, E25.399604; Fig. 6d). The sill is folded about a NE–SW trending axis with the host granodiorite, and may constrain the timing of E–W deformation assuming it was emplaced in-situ and paleo-horizontal; alternatively, it could represent an enclave of an earlier intrusion.

Delos Leucogranite Samples

17TL95 biotite-tourmaline leucogranite sill intrudes parallel to the sillimanite-grade gneissic foliation on the eastern coast of Delos (N37.406523, E25.266933). The sill and the surrounding rocks locally exhibit complex relationships with hornblende-biotite granitoids that cross-cut the gneissic foliation and the leucogranites (Fig. 4b).

Table S7: Sample locations and descriptions

Sample Name	Rock Type	Island	GPS Location	Description
TLT64	Dacite Dyke	Tinos	N37.628196, E25.164215	Lightly recrystallized dyke in Upper Unit NE of Kolimpithra, cross cutting the foliation associated with TSZ.
17TL36	Dacite Dyke	Tinos	N37.580526, E25.23496	Undeformed dyke intruding gabbros and periodotites of the Tsiknias Ophiolite on the eastern Mt Tsiknias. Fine grained groundmass with subangular to rounded plagioclase

				phenocrysts and little quartz, similar mineralogy to TLT64.
17TL05	Dacite Dyke	Tinos	N37.553558, E25.134661	Slightly more evolved dacite dyke with more plagioclase in the groundmass, undeformed and cross-cuts top-to-SW blueschist facies fabrics at Kionnia Bay. Striking ~360 dipping ~30° East, approximately 10 m wide.
TLTN34	Deformed monzogranite	Tinos	N37.582732, E25.175706	Deformed south margin of the Tinos I-type granite pluton, at road cutting, hornblende defines lineation plunging ~040/10.
TLTN36	Undeformed monzogranite	Tinos	N37.596171, E25.197489	Undeformed granite within the interior of pluton, coarsely crystalline with plagioclase, quartz, k-feldspar phenocrysts and hornblende, minor biotite, titanite.
TLT13	Aplite vein	Tinos	N37.583181, E25.20910	Leucocratic aplite vein ~3 cm wide intruding into Mirsini Unit (sub ophiolitic sole pelagic rocks), with dominantly plagioclase and quartz and minor hornblende.
TLTN13	Grt-Ms Leucogranite	Tinos	N37.612741, E25.242176	Fine grained leucogranite sill, dominantly plagioclase with garnet up to 1-2 mm in diameter and fine grained muscovite approximately 2m wide intruding amphibolites from Tsiknias metamorphic sole at Livada Bay and cross-cut by high angle normal faults with offsets ~1-2 m.
TLTN15	Grt-Ms Leucogranite	Tinos	N37.613210, E25.244438	Another garnet-muscovite leucogranite sill further along the same outcrop at Livada Bay with almost identical composition to TLTN13 but appears to rotate slightly into alignment with normal faults. Normal faults cross cutting strike ~330 dipping ~60 ° to ENE.
17TL100	Cross-cutting leucogranite	Tinos	N37.610512, E25.236602	Biotite leucogranite vein swarm approximately 2-10 cm wide, striking ~109 ° and orientated subvertical on the eastern margin of Tinos I-type pluton at Livada Beach

17TL95	Delos Bt-Tur Leucogranite	Delos	N37.406523, E25.266933	Leucogranite sill, cross cutting biotite-sillimanite gneisses. Subparallel to foliation, and possible evidence for magma mixing with I-type Hb-Bt intrusion.
TL57	Orthogneiss Basement	Naxos	N37.06696 E25.44710	Banded biotite gneiss, including k-feldspar, plagioclase, quartz, minor sillimanite, ilmenite.
TL58	Grt-Bt Leucogranite dyke	Naxos	N37.118726 E25.527931	Undeformed leucogranite on eastern side of migmatite dome, cross-cutting top-to-NNE fabrics associated with KSZ.
TL63	Grt-Tur leucogranite	Naxos	N37.094362, E25.443100	Steep branching leucogranite dyke ~3 m wide with branching dykes cross-cutting steep metamorphic foliation and top-to-NNE shear fabrics associated with the NPDS. General dyke geometry however subparallel to the metamorphic foliation striking ~190°/80° to west.
TL69	Grt-Tur-Ms leucogranite	Naxos	N37.13789 E25.46937	Deformed leucogranite, aligned with steep fabrics dipping ~50 ° to west associated with NPDS.
TL72	Deformed Grt-Tur leucogranite	Naxos	N37.183593, E25.506738	Deformed and boudinaged leucogranite sill, aligned with NPDS shear fabrics and adjacent with sheared serpentitized peridotite lense within the highly deformed NPDS shear zone on the NW coast road. The solid-state deformation suggests it intruded prior to top-to-NNE shearing and steep doming on the NPDS.
TLN8	Bt-Tur leucogranite	Naxos	N37.106069, E25.482802	Horizontally boudinaged dyke within calcite marbles in the core-high-strain zone at the center of the migmatite dome. Dyke strikes 010 and is vertically dipping with post-crystallization boudinage along its strike. Marbles with tremolite and diopside deform around the boudinaged pieces, suggesting NNE-SSW extensional deformation occurred at high-temperature when amphibole behaves ductile (>600 °C). Amphibolite

				layers also affected by brittle domino type boundinage along the same direction.
TLN10	Bt-Ms leucogranite in core high strain zone	Naxos	N37.106169, E25.482779	Vertically boudinaged Leucogranite dyke within the core high strain zone at the center of the Naxos migmatite dome. The dyke trends 010 and is vertically dipping within calcite marbles and is affected by ductile but solid-state post crystallization boudinage, with stretching in the vertical direction.
17TL106	Aplite within Granodiorite	Naxos	N37.074694, E25.399604	Folded leucocratic aplite, dominantly plagioclase and quartz with minor biotite ~50 cm wide within the west Naxos Granodiorite pluton within 600 m of the eastern margin of the pluton, in the village of Glinado to the east of the main road entering the village. The aplite appears to be uprightly folded in an open synform also with the host granodiorite also folded. The fold axes strikes ~170, dipping sub vertically.

References

- Abbey, S., (1983), Studies in "Standard Samples" of silicate rocks minerals 1969-1982: *Geological Survey of Canada Paper* v. 83-15, pp. 1-114.
- Govindaraju, K., (1994). 1994 Compilation of Working Values and Sample Description for 383 *Geostandards: Geostandards Newsletter*, v. 18, Special Issue, pp. 1–158
- Hiess, J., Condon, D. J., McLean, N., & Noble, S. R. (2012). 238U/235U systematics in terrestrial uranium-bearing minerals. *Science*, v. 335(6076), pp.1610–1614.
- Harris, N.B., Pearce, J.A. and Tindle, A.G., (1986). Geochemical characteristics of collision-zone magmatism. Geological Society, London, Special Publications, 19(1), pp.67-81.
- Horstwood, M. S. A., Košler, J., Gehrels, G., Jackson, S. E., McLean, N. M., Paton, C., Pearson, N. J., Sircombe, K., Sylvester, P., Vermeesch, P., Bowring, J. F., Condon, D. J. and Schoene, B. (2016). Community-Derived Standards for LA-ICP-MS U-(Th-)Pb Geochronology – Uncertainty Propagation, Age Interpretation and Data Reporting. *Geostand Geoanal Res*, v. 40, pp. 311–332. doi:10.1111/j.1751-908X.2016.00379.x

- Ludwig, K., 2003a, ISOPLOT 3.00: a geochronology toolkit for Microsoft Excel, *Berkeley Geochronological Center Special Publication*, Berkeley (2003)
- Ludwig, K., (2003b), Isoplot/Ex Version 3.00: a geological toolkit for Microsoft Excel, *Berkeley Geochronology Center Special Publication*, v. 4, pp. 70
- McArthur, J.M, Howarth, R.J., and Bailey, T.R. (2001) Strontium isotope stratigraphy: LOWESS Version 3: Best fit to the marine Sr-isotope curve for 0-509 Ma and accompanying look-up table for deriving numerical age. *J. Geol.* 109, 155-170.
- Münker, C., Weyer, S., Scherer, E., Mezger, K., (2001). Separation of high field strength elements (Nb, Ta, Zr, Hf) and Lu from rock samples for MC-ICPMS measurements. *Geochem. Geophys. Geosyst.* 2. doi:10.1029/2001GC000183.
- Nowell, G.M. & Parrish, R.R. (2001). Simultaneous acquisition of isotope compositions and parent/daughter ratios by non-isotope dilution-mode plasma ionisation multi-collector mass spectrometry (PIMMS). In *Plasma Source Mass Spectrometry: The New Millennium* (Holland, G. & Tanner, S.D. eds) *Royal Soc. Chem., Spec. Publ.* v. 267, pp. 298–310.
- Reichen, L.E. and Fahey, J.J., (1962). An improved method for the determination of FeO in rocks and minerals including garnet. *U.S. Geological Survey Bulletin*. V. 1144B, pp. 1–5.
- Retzmann, A., Zimmermann, T., Profrock, D., Prohaska, T., and Irrgeher, J. (2017) A fully automated simultaneous single-stage separation of Sr, Pb, and Nd using DGA Resin for the isotopic analysis of marine sediments. *Anal. Bioanal. Chem.* 409, 5463-5480.
- Romaniello, S.J., Field, M.P., Smith, H.B., Gordon, G.W., Kim, M.H, and Anbar, A.D. (2015) Fully automated chromatographic purification of Sr and Ca for isotopic analysis. *J. Anal. At. Spectrom.* 30, 1906-1912.
- Pearce, P.A., Harris, N.B.W., and Tindle, A.G., (1984). Trace element discrimination diagrams for the tectonic interpretation of granitic rocks: *Journal of Petrology*, v. 25, p. 956-983, doi:10.1093/petrology/25.4.956.
- Spencer, C. J, Cawood, P. A, Hawkesworth, C. J., Prave, A. J., Roberts, N. M. W., Horstwood, M. S. A., Whitehouse, M. J., (2015). Generation and preservation of continental crust in the Grenville Orogeny, *Geoscience Frontiers*, v. 6, pp. 357–372.
- Stacey J. S. and Kramers J. D., (1975). Approximation of terrestrial lead isotope evolution by a two-stage model. *Earth and Planetary Science Letters*, v. 26, pp. 207–221.
- Tanaka, T., Togashi, S., Kamioka, H., et al. (2000) JNdi-1: a neodymium isotopic reference in consistency with LaJolla neodymium. *Chem. Geol.* 168, 279-281.

Weis, D., Kieffer, B., Maerschalk, C., Barling, J., de Jong, J., Williams, G.A., Hanano, D., Pretorius, W., Mattielli, N., Scoates, J.S., Goolaerts, G., Friedman, R.M., and Mahony, J.B. (2006) High-precision isotopic characterization of USGS reference materials by TIMS and MC-ICP-MS. *Geochem. Geophys. Geosyst.* 7, Q08006.

Vermeesch, P., 2018, IsoplotR: a free and open toolbox for geochronology. *Geoscience Frontiers*, v.9, p.1479-1493, doi: 10.1016/j.gsf.2018.04.001.